

VISUALIZATION OF THE EVAPORATION AND CONDENSATION PHENOMENA IN CRYOGENIC PROPELLANTS

Kishan Bellur,¹ Vinaykumar Konduru,¹ Ezequiel F. Médici,¹
Daniel S. Hussey,² David L. Jacobson,² Jacob M. LaManna,²
Jeffrey S. Allen,¹ & Chang Kyoung Choi^{1,*}

¹Michigan Technological University, Houghton, MI, 49931, USA

²National Institute of Standards and Technology, Gaithersburg, MD, 20899,
USA

*Address all correspondence to: Chang Kyoung Choi, Michigan Technological University,
Houghton, MI, 49931, USA, E-mail: cchoi@mtu.edu

Prediction and control of evaporation/condensation of cryogenic propellants is one of the key factors limiting long-term space missions. Modeling propellant behavior and predicting phase change rates require models that need to be calibrated with experimental data. However, no such data is available on controlled phase change of cryogenic propellants. In this work, neutron imaging is employed as a means to visualize the condensed propellant inside opaque metallic containers at temperatures as low as 17 K. By controlling the temperature and pressure, a wide variety of phase change rates could be obtained. An exponential attenuation model is used to accurately determine the liquid–wall interface. Two methods of determining liquid volume as a function of time are described and compared. The interface tracking method uses an adaptive threshold edge detection and fit to the Young–Laplace equation while the optical density method calculates the liquid thickness for every pixel based on the Beer–Lambert law with a beam hardening correction. The former method is applicable only in images that have a fully formed meniscus whereas the latter method can be used on all images despite the shape/location of the liquid in the cell. Uncertainty in volume measurement with the optical density method is 6% lower than with the interface tracking method, and the results are in excellent agreement. In addition to volume, optical density method can be used to measure thickness of the thin liquid film on the wall of the container. For steady states, the interface tracking method will suffice but the optical density method is useful for high-accuracy volume measurements and thin film analysis.

KEY WORDS: *evaporation, condensation, neutron imaging, cryogenic propellants, liquid hydrogen, liquid methane*

1. INTRODUCTION

One of the key challenges in long-term space missions is the ability to store and predict evaporation and condensation of cryogenic propellants. The most commonly used propellants are liquid hydrogen and methane that must be stored at temperatures as low as 20 K and 110 K, respectively, under atmospheric pressure, to prevent boil off. The propellants are extremely sensitive

to temperature/pressure variations and undergo phase change, even in space, resulting in self pressurization of tanks. Long-term storage and transfer of propellants are mission critical technologies at NASA (Council, 2012). Computational fluid dynamics (CFD) models have been used to predict the pressure and behavior of the cryogenics inside large tanks and it was found that a thin (≈ 1 mm) liquid film exists between the vapor and the solid phase (Barsi et al., 2005; Panzarella and Kassemi, 2003, 2005, 2009; Panzarella et al., 2004). Several bubble point pressure and vapor breakthrough experiments conducted at NASA Glenn suggest that the understanding of local thermodynamics is critical and much of the uncertainty was attributed to phase change (Hartwig and McQuillen, 2011, 2012; Hartwig et al., 2013). The type of phase change encountered here is different from pool boiling and depends on several other factors in addition to temperature and equilibrium vapor pressure. The curvature of the liquid meniscus near the contact line results in an anisotropy in the liquid stresses including a pressure jump at the interface due to the surface tension. The intermolecular forces between the solid phase and the liquid become important in this thin film and give rise to a net pressure drop (disjoining pressure effect). As a result of these factors, the evaporation is nonuniform and most of the evaporation occurs in the thin liquid film called the contact line region. For wetting fluids, it has been shown that 60–90% of the evaporation occurs in the contact line region (Fritz, 2012; Panchamgam et al., 2008; Plawsky et al., 2008; Wee et al., 2006). Hence, the experimental effort to measure evaporation must focus on visualization and accurate determination of the liquid–vapor interface, especially in the contact line region.

Curvature and disjoining pressure effects have been incorporated in some phase change models (Ajaev, 2012; Plawsky et al., 2008; Preiss and Wayner, 1976; Wayner, 1991), but the results involve fitting the model's results to experimental data. Accurate modeling is still a challenge due to the lack of reliable experimental data on controlled phase change of cryogenic propellants (Alberts et al., 2015, 2016; Panzarella and Kassemi, 2009). Controlled experimental evaporation/condensation tests of cryogenic propellants are difficult to perform due to the fact that conventional visualization techniques cannot be used to image liquids inside metallic containers. Cryogenic propellants such as hydrogen and methane undergo phase change at 20 K and 110 K, respectively, at atmospheric pressures. During evaporation, the pressure builds up and a sophisticated manifold with a control system is necessary to control both pressure and temperature inside the metallic container. Further, flash evaporation of highly combustible propellants such as hydrogen invoke safety issues that require extreme caution during experiment design.

In the present study, neutron imaging is used as a visualization technique to detect the condensed propellant inside cylindrical Al 6061 test cells. Propellant vapor is introduced at a preset pressure into a cryostat cooled by liquid helium and liquid nitrogen. Condensation is achieved in the test cell by dropping the cryostat temperature lower than the saturation temperature and subsequent evaporation is achieved by raising the cryostat temperature above the saturation temperature. These tests were conducted at the BT-2 neutron imaging facility at the National Institute of Standards and Technology (NIST) at Gaithersburg, MD. This article details the visualization technique employed to capture the liquid–vapor interface and image analysis to obtain the phase change rates.

1.1 Neutron Imaging

Using neutrons for imaging can be dated back to the 1940's (Hartmut and Ernst, 1940) but it was during the advances in digital photography and image processing that it became popular as a reliable tool for nondestructive testing (Körner, 2000). Although the resolution obtained

from neutron imaging is currently limited to about 10 μm , the capability to easily record and manipulate image data for 3D tomography studies spurred the development of digital neutron imaging. Brenizer (2013) provides an extensive review of neutron imaging from its conception to the present day. Neutrons have no charge and interact with matter through the strong nuclear force, and as a result have good penetrating power through most metals. Neutrons do not deposit appreciable energy into a sample (if the entire beam was absorbed, the energy is of order $\mu\text{W}/\text{cm}^2$). Neutron imaging is a radiographic technique similar to X-rays, which makes use of the differences in attenuation characteristics of different elements (Von der Hardt and Röttger, 2012). Neutron interaction with matter can be broadly classified in 3 ways: (1) scattering due to interaction with the sample atoms, (2) absorption by the nucleus, and (3) transmission through the interstitial spaces between the atoms. Neutron scattering and absorption are characterized by cross sections (σ). The cross section is a probability expressed in units of area that denotes the likelihood of the neutron interaction with the medium of interest (Fig. 1). Cross sections can be defined for both absorption (σ_a) and scattering (σ_s). The intensity of transmitted neutrons obeys the Beer–Lambert law of exponential attenuation:

$$I = I_0 e^{-\mu d}. \quad (1)$$

In Eq. (1), I_0 is the intensity of the incident beam, μ is the macroscopic cross section (also known as attenuation coefficient) given by $\mu = n\sigma$, $\sigma = \sigma_a + \sigma_s$, n is the number density given by $n = (\rho A)/M$, ρ is the density of medium, A is the Avogadro number, M is the molar mass, and d is the thickness of the medium. Thermal neutrons are almost transparent to many metals but are strongly attenuated by light atoms such as hydrogen, lithium, and boron. Table 1 compares the scattering lengths and attenuation coefficients of hydrogen, aluminum, iron, and carbon. All hydrogenated compounds such as methane also exhibit strong neutron attenuation. It is this difference in attenuation coefficients that allows for the visualization of the liquid propellant meniscus through an aluminum cylinder. Neutron imaging allows not only for qualitative measurements but also quantitative measurements of the meniscus shape. Neutron imaging has successfully been used in a variety of liquid detection applications such fluid transport in porous media (Dewanckele et al., 2014; Kang et al., 2013; Perfect et al., 2014), fuel cells (Bazylak, 2009; Kramer et al., 2005; Satija et al., 2004), and heat pipes (Cimbala et al., 2004; Kihm et al., 2013; Wilson et al., 2008). To the authors' best knowledge, these are the first known neutron images of cryogenic propellant phase change.

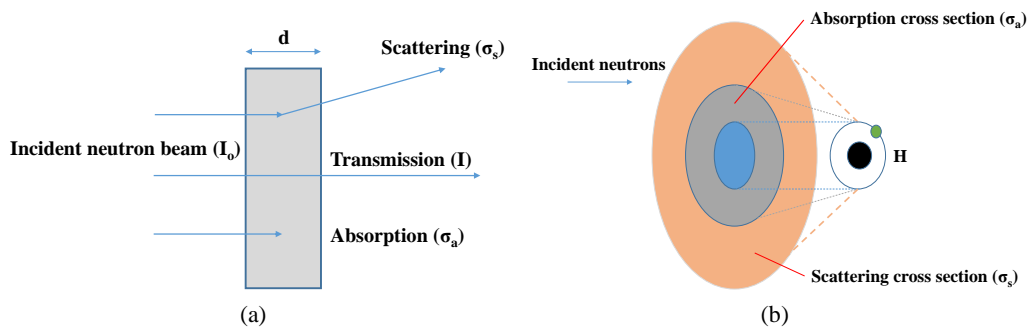


FIG. 1: Neutron interaction with matter and cross sections. (a) Neutron interaction with matter, (b) absorption and scattering cross sections

TABLE 1: Neutron cross sections and attenuation coefficients for 20 meV neutrons (second column values based on Chadwick et al., 2006)

Species	σ (b)	Density (g/cm ³)	μ (cm ⁻¹)
Hydrogen (liquid)	33.75	0.0707	1.437
Hydrogen (vapor)	33.75	0.0013	0.026
Aluminum	1.34	2.7	0.083
Carbon	5.02	2.25	0.566

The objective of the current study is to establish a method to accurately determine the phase change (evaporation/condensation) rates by measuring the liquid propellant volume in every image. Two different methods are employed to measure volume: (1) interface tracking method and (2) optical density method. The interface tracking method involves using traditional image processing concepts such as spatial filtering and edge detection. The shape of the liquid vapor interface is determined, and the interface is tracked as a function of time to calculate the liquid volume. The optical density method uses the beam hardness corrected Beer–Lambert law [Eq. (1)] to transform every pixel's gray value into a liquid thickness from which the volume is computed.

2. EXPERIMENT

2.1 Test Setup

A 70 mm cryostat was used to cool and eventually condense the propellant vapor introduced into the test cell. The cryostat consists of annular rings filled with cryogenics with the test cell at the center in a space called the "sample well." The cryostat is cooled by an outer jacket of liquid nitrogen that is constantly boiling at atmospheric pressure maintaining a constant temperature of 77 K. An inner jacket is filled with liquid helium that also undergoes phase change by throttling. The vaporization of liquid helium cools a copper heater block that in turn cools the cryostat's sample well. The vaporized helium then rises up the innermost annulus cooling the entire inner wall of the cryostat. The helium vapor is then either removed by a vacuum pump or vented to the ambient atmosphere depending on the cooling rate needed. The throttle valve and a helium exhaust valve serve as a means of controlling the vapor pressure and hence the cooling power of the cryostat. The cryostat is being cooled constantly as long as the cryogenics are replenished. The copper heat exchanger has a temperature sensor and an electric heater embedded in it. Steady state operation is obtained by matching the electric heater power to the cooling power from the cryogenics.

The test cell is mounted to a long hollow stainless steel sample stick by use of a custom fabricated SS 316 lid and inserted into the cryostat's sample well (Fig. 2). The lid has a 1/8" male VCR fitting brazed to its side to allow for connection to a vapor feed line. An internal groove then transfers the vapor from the feed line to through the lid and into the test cell. The lid is connected to the test cell by use of 6 Al 4-40 screws and an indium O-ring. The entire setup and all fittings were helium leak checked prior to testing. The instrumented sample stick is inserted into the cryostat while the sample well is being flooded with helium vapor about 135 kPa. Helium flooding of the sample well is essential to prevent the introduction of ambient air along with the sample stick. Once the stick is inserted, it is secured with an O-ring seal and the sample well is pumped down to a pressure of 10^{-3} Pa to remove any traces of other gases

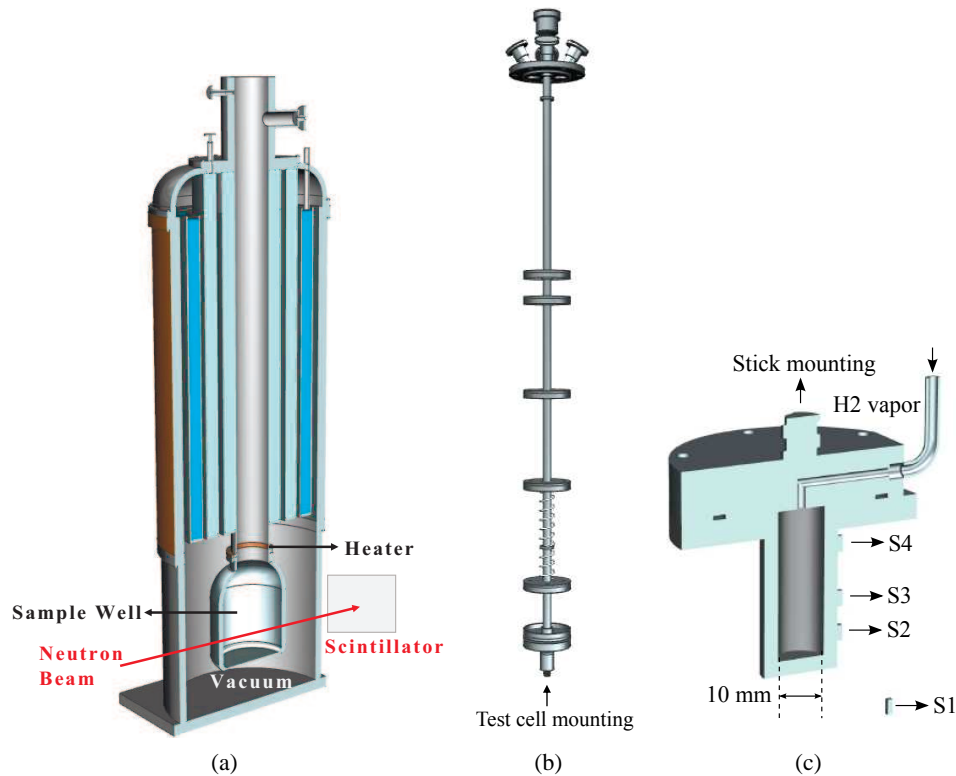


FIG. 2: Test setup showing the instrumented test cell attached to the end of a long SS sample stick which inserted into the sample well of the 70 mm “orange cryostat.” (a) 70 mm cryostat, (b) sample stick, (c) 10 mm Al 6061 test cell

that might be present. Helium vapor is reintroduced into the sample at 135 kPa and the process is repeated at least 3 times. After the final evacuation, a small amount of helium is added to act as a heat exchange gas between the sample well and the copper heat exchanger/cryostat inner wall. The amount of helium added determines the transient thermal response between the heat exchanger and the test cell. During the time of the experiments, the final helium pressure in the sample well could not be measured. Numerical simulations are being conducted by the authors to characterize the thermal response and will be published in a future article. The stick contains several radiation baffles to prevent heat leaks by radiation from the top flange.

Three Lakeshore silicon diode DT-670 (S2–S4) sensors are mounted on the outside of the test cell by use of Kapton tape and were secured in place by use of custom made stainless steel springs. A fourth sensor (S1) is suspended in the helium exchange gas close to the test cell (Fig. 2). The DT-670 sensors were connected to a Lakeshore model 340 temperature controller for data logging. The corresponding calibration curves for DT-670 sensors are built into the temperature controller. The temperature of the copper heat exchanger (NTC RTD X45720 sensor embedded in the heater housing) of the cryostat and the stick temperature (Si410B sensor embedded into the bottom of the stick) is logged by a Lakeshore model 331. Auto PID closed loop control is set up for the cryostat’s copper block temperature. All tests were conducted at a 5 W maximum setting. The uncertainty in the DT-670 temperature measurements is ± 0.25 K. The

uncertainty in the cryostat heat exchanger temperature is ± 0.1 K. The pressures are logged by two independent pressure transducers. One transducer (Mensor CPG 2500) was connected to the feed line and the other transducer (Mensor DPG 15000) was connected to the manifold. The uncertainty in the pressure measurements was 0.2% at 100 kPa, increasing to 1% at 25 kPa. The computer used for data logging was a Windows XP SP3 machine running Intel Xenon X5550 @ 2.67 GHz, 4 GB RAM and 2TB hard drive. The Lakeshore controllers and pressure transducers are connected to the logging computer via serial ports and data is logged every second. Additional details on the experimental setup can be found at Bellur et al. (2016b).

2.2 Imaging Setup

The sample stick-test cell assembly after being inserted into the cryostat is placed in the collimated neutron beam such that the center of the beam passes through the center of the test cell. A scintillator (screen that captures neutrons and emits photons along with gamma radiation) is placed downstream to detect neutron transmission (Fig. 2). The scintillator used was a 7.6 mg/cm^2 Gadoxysulfide screen that had a thickness of $20 \text{ }\mu\text{m}$. The visible (green) light emitted by the scintillator is captured by an Andor NEO sCMOS (scientific Complementary Metal Oxide Semiconductor) camera with a pixel pitch of $6.5 \text{ }\mu\text{m}$ with variable exposure time. An 85 mm Nikon lens with a PK 13 extension tube was used to focus the scintillator light onto the camera. The experiments were conducted at the Neutron Imaging Facility (NIF) NIST Center for Neutron Research (NCNR) in the BT-2 thermal beam line. Details on the NIF facility and the beamline layout can be found in Hussey et al. (2005, 2010).

The generation of the neutron beam is an inherently random process, so that the statistics of the image formed by the neutron beam are well described by a Poisson distribution. The standard deviation of this distribution reduces with exposure time at the expense of temporal resolution (Kramer et al., 2005). An exposure time of 10 s was found to be an appropriate compromise for the phase change rates being tested and the liquid interface moves by no more than 15 pixels in two consecutive images. The image formation process is well described by pinhole optics and geometric blur arises as a result. Further, the detector resolution can limit the spatial resolution. The image can be enhanced by deconvolution with an estimated point spread function (PSF) determined from a sharp edge on the image as described by Hussey et al. (2010). The estimated PSF and the results of deconvolution is discussed in a later section.

During the experiment, images are captured while saturated vapor at a constant pressure is introduced into the test cell and the cryostat temperature is lowered to achieve condensation of the propellant. When sufficient condensation is obtained, the cryostat temperature is then increased above the saturation condition to achieve evaporation. The imaging is stopped when all the liquid has evaporated. During every test, images were captured with the neutron beam turned off, in order to characterize the background radiation from the reactor. The attenuation coefficient of hydrogen is almost 56 times greater than that of aluminum. Hence the neutrons easily pass through the aluminum container but are then blocked by the hydrogen. The high neutron cross section of the liquid propellant in comparison to both the containment vessel material and propellant vapor allows for the visualization of the liquid.

3. IMAGE PREPROCESSING

The images obtained from the camera are stored as single precision 32 bit FITS images with an imaging array size of 2160×2560 pixels. The pixel gray values represent neutron transmission

intensities as observed from the scintillator light. Figure 3 shows a condensation/evaporation test from January 2015. The hydrogen vapor was set at a constant pressure of 120.6 kPa corresponding to a saturation temperature of 21 K. Temperature of the cryostat was lowered to 19 K for condensation and increased to 23 K for evaporation. The dark region of the captured images represents low neutron transmission (liquid propellant) while the bright regions represent high neutron transmission (metals and propellant vapor).

Prior to using any method to determine the liquid volume, several parameters such as the location of the liquid–wall interface, pixel pitch and inherent rotation of the image must be determined and accounted in the forthcoming analysis. These preprocessing routines are common between both volume determination methods: interface tracking method and optical density method.

3.1 Liquid–Wall Interface

Accurate determination of the liquid–wall interface location is vital for the curvature fitting with the interface tracking method and volume measurements with both methods. Assuming the outer wall of the cryostat and helium vapor does not significantly affect the neutron intensities, the attenuation due to thickness of liquid, and the test cell wall can be modeled using the Beer–Lambert’s law [Eq. (1)]. The pixel intensities of the wall region are first fitted with an exponential model [Eq. (1)]. The results of this fit are then applied to the liquid region where the neutrons travel through both the test cell wall and the liquid. This is done using a two term exponential model where one term represents the test wall thickness and the other term represents the liquid thickness. The point of intersection of the liquid and the wall fits are evaluated as shown in Fig. 4(a). The plot represents exponential fits to the pixel intensities shown by the red line and arrow in Fig. 4(b).

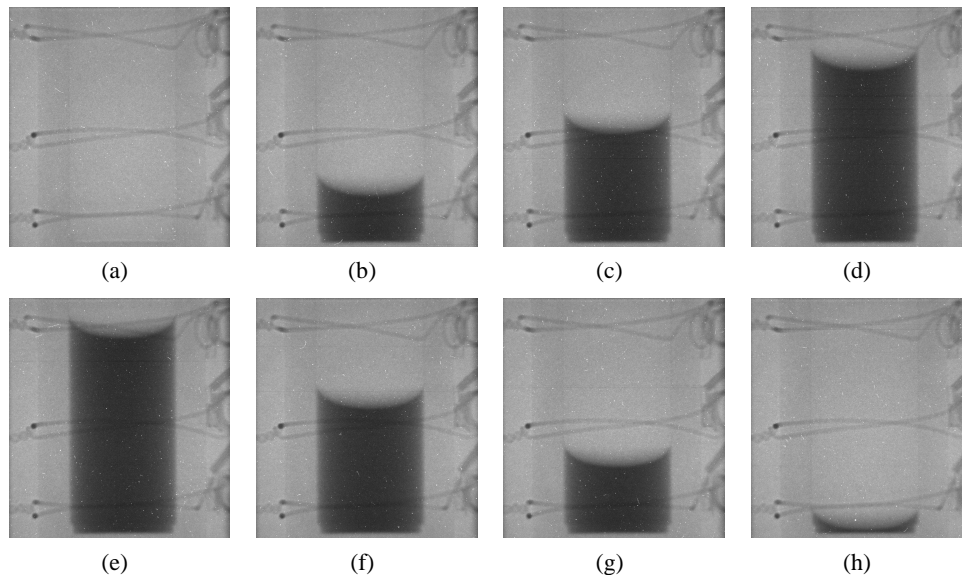
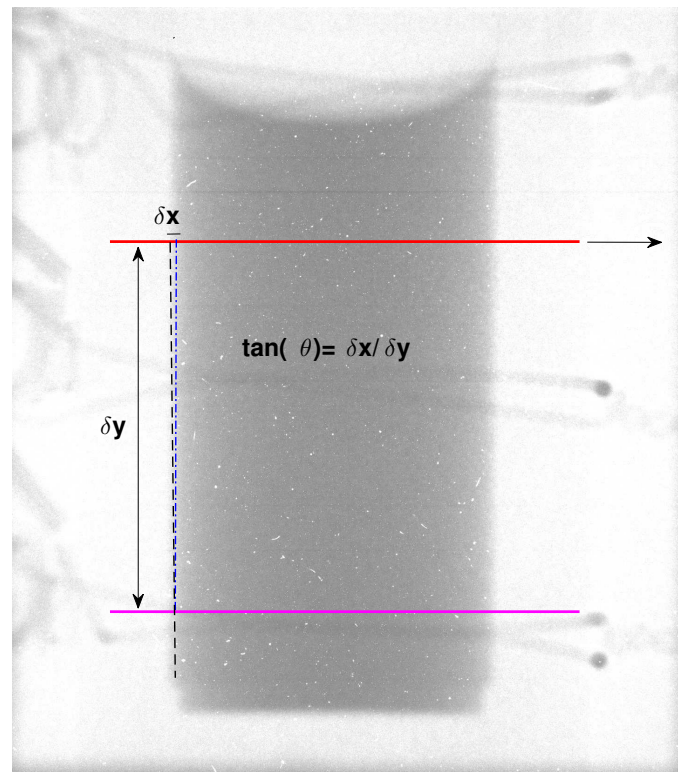
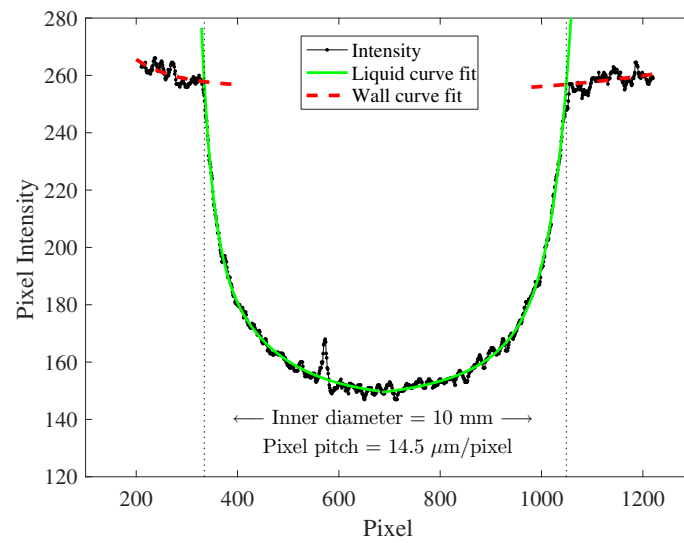


FIG. 3: Time lapse images of liquid hydrogen phase change in the 10 mm Al 6061 test cell. (a) 11 s, (b) 997 s, (c) 1218 s, (d) 1438 s, (e) 2654 s, (f) 3316 s, (g) 3867 s, (h) 4475 s



(a)



(b)

FIG. 4: Determination of (a) rotation and (b) liquid–wall interface and pixel pitch using pixel intensities shown by the red (top) line and arrow. The image represents liquid hydrogen at 21 K in the 10 mm Al 6061 test cell

3.2 Pixel Pitch

A correlation between the actual physical dimension and the pixel size is essential for any data analysis. Since the sample geometry was accurately machined and measured, it was used to calculate the effective pixel pitch. This is done by counting the number of pixels that make up the diameter of the test cell and scaling the obtained number by the measured diameter of the test cell. This was done for 10 images and at 5 different locations chosen at random on the test cell and then averaged. The effective pixel pitch was found to be 14.4 μm per pixel for the January 2015 tests and 16.5 μm per pixel for the September 2016 tests. Figure 4(b) shows the pixel pitch for the January 2015 setup.

3.3 Image Rotation

In order for the interface tracking and the curvature determination to be accurate, the images containing the test cell and liquid meniscus must be as vertical as possible. An error of 0.5° in rotation results in an increase of the corresponding volume measurement by up to 2% and the measured contact angle by up to 5° . The rotation was determined by analyzing images that have cryogenics filled almost to the top of the vessel. The relative distance between the wall coordinates determined by analyzing points of the highest gradient was logged and measured for a sample of images. A correlation between the relative drift in the x coordinate (δx), at various δy distances was obtained. The slope of the linear fit of δx vs. δy is the tangent of the rotation angle. The rotation angle determined from image preprocessing is about 0.12° for the January 2015 tests and 0.41° for the September 2016 tests.

3.4 Deconvolution

Assuming the test cell is perfectly aligned in the beam, the inner bottom center edge of the test cell was analyzed to determine the imaged width of the assumed sharp edge. This spread of pixel intensities was fitted to a Gaussian distribution and it was found that the standard deviation was about 3.5 pixels. Hence a symmetric Gaussian PSF with a standard deviation of 3.5 was used to deconvolve the images with 3 iterations of the Richardson–Lucy algorithm in MATLAB.

4. IMAGE ANALYSIS

4.1 Interface Tracking Method

The interface tracking method is an extension of the curvature measurement technique that involves an adaptive threshold edge detection and is validated by a fit to the theoretical Young–Laplace curve. Determining the liquid–vapor interface shape and tracking the interface in every image involves considerable spatial filtering in addition to the deconvolution to account for inherent noise in the neutron images. Although the image is a 32 bit image, it was determined that the pixel gray levels of importance are between 100 and 340. The original neutron images, however, contain several spots of intensities (gray levels) well above 20,000 due to intrinsic noise in the camera or deposition of energy into the sensor from gamma rays. These intensities are essentially background noise and can be removed by using a spatial median filter. The pixel intensity histogram (Fig. 5) shows 3 peaks at about 160, 240, and 260 corresponding to liquid hydrogen, aluminum wall, and hydrogen vapor. In order to avoid unnecessary blurring of the image instead

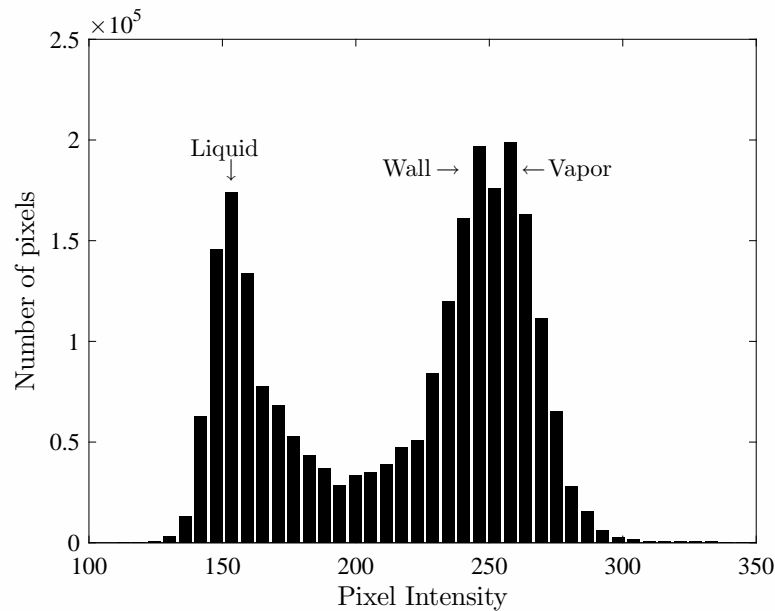


FIG. 5: Histogram of pixel intensities for a typical liquid hydrogen in Al 6061 neutron image

of using a spatial median filter, intensities above 340 are set to 340, and all intensities were subtracted by 100 to remove the initial offset.

Upon initial investigation it was observed that the curvature of the liquid–vapor interface does not change considerably with evaporation or condensation even though the contact line is moving. This is due to the slow phase change rates in the experiment in conjunction with the spatial resolution limits of the imaging setup. Any curvature change with contact line motion would require spatial resolution less than $5\ \mu\text{m}$. Hence, the signal to noise ratio in the captured images could be enhanced by image stacking. This is done by tracking the lower apex of the meniscus and cropping out the liquid–vapor interface in every image. The cropped images are then aligned, stacked, and averaged to remove gamma noise. Salt noise was removed by using a 5×5 median filter prior to stacking. The final image obtained (Fig. 6) has high signal to noise ratio so that edge detection and a Laplace fit can be performed.

The liquid–vapor interface has a three dimensional curvature with contribution from both the in plane and the through plane components. Hence, a 1D edge detection does not suffice. The liquid–vapor interface region looks smeared because the image is essentially a shadow graph and the intensity reduces exponentially with film thickness and eventually becomes smaller than the resolution of the detector system. The pixel intensities change in both directions of the obtained 2D image. Variation in the vertical direction is due to reducing film thickness and intensity changes in the horizontal direction are due to the cylindrical geometry of the sample. In such a case, if a constant limiting intensity threshold is used, it would result in an erroneous meniscus shape. In order to overcome these challenges, a unique curvature determination is employed using an adaptive threshold. The preprocessed parameters along with the stacked images are used in a preliminary 1D vertical scan to obtain the first guess of the liquid–vapor interface. Based on the initial scan, the 2D meniscus is divided into 3 zones for processing: (1) a central zone where the curvature variation is small owing to the flat interface in the center, (2) an intermediate zone,

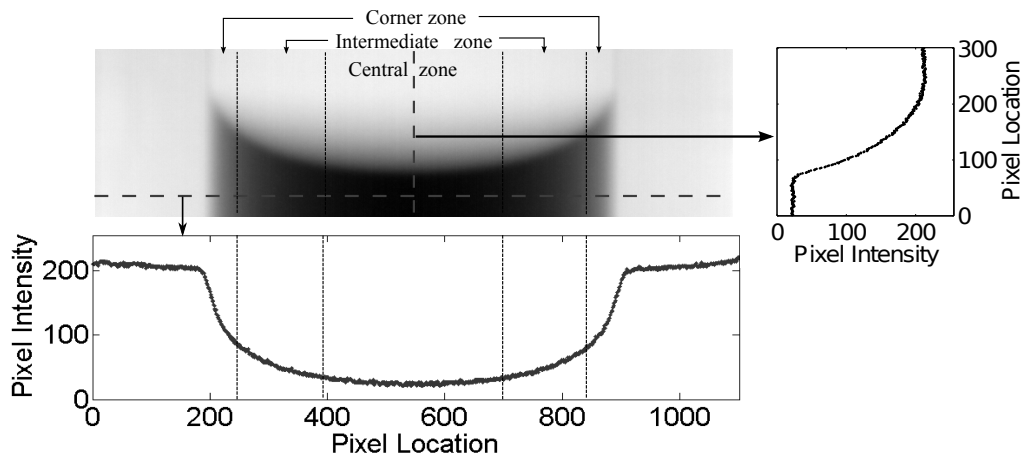


FIG. 6: Stacked image showing the three zones of analysis, horizontal and vertical intensities along the centerline

where the 2D curvature changes significantly, and (3) a corner zone where the curvature variation drops again, and the film thickness is lower than ≈ 2 mm. The image is sliced vertically and the three zones are analyzed separately (Fig. 6).

All the pixels in the central zone are processed through a vertical 1D median filter of size 10 and a vertical 1D sgolay filter of size 10 in MATLAB and then averaged to remove any remaining neutron noise. A 1D vertical scan is made along every pixel column to find the first pixel location whose intensity is equal to the average intensity of the liquid region pixels in the same column. Hence, the limiting intensity constantly changes and results in an adaptive threshold. This adaptive threshold method accounts for the horizontal intensity smear as one gets closer to the wall. A quadratic curve fit to this edge provides a more accurate representation of the meniscus in the central zone. The ends of the quadratic fit serve as initial parameters for the intermediate zone left of the central zone. A diagonal edge detection is performed by scanning in both the x and y coordinates to find pixel positions that have intensities equal to the average intensity of all the liquid region pixels in the particular column directly underneath the current x range. Hence a modified adaptive threshold method is used in the intermediate zone to account for both the vertical and horizontal intensity distribution. The end point of the intermediate zone serves as an initial point for the left corner zone. The corner zone is analyzed using a 1D horizontal scan and the adaptive threshold method. The process is repeated for the right intermediate and the right corner zones. The resulting pixel location and intensities are extracted and a cubic spline fit is performed to ensure continuity between the zones. The final edge detected interface is shown in Fig. 7.

The obtained edge detected interface is scaled and curve fitted to a theoretical Young–Laplace curve for validation. The Young–Laplace equation for an axisymmetric cylinder in cylindrical coordinates is given by the following equation (Concus, 1968):

$$\frac{df(\psi)}{d\psi} = \frac{\sin \psi}{\text{Bo}f - (\sin \psi)/r + \lambda}, \quad \frac{dr(\psi)}{d\psi} = \frac{\cos \psi}{\text{Bo}f - (\sin \psi)/r + \lambda}, \quad (0 < \psi < \frac{\pi}{2} - \theta). \quad (2)$$

Additional conditions at the ends are given by $f(\psi) = r(\psi) = 0$ at $\psi = 0$ and $r(\psi) = 1$ at $\psi = \pi/2 - \theta$. The apex is taken as the origin of the coordinate system. The quantity $f(r)$

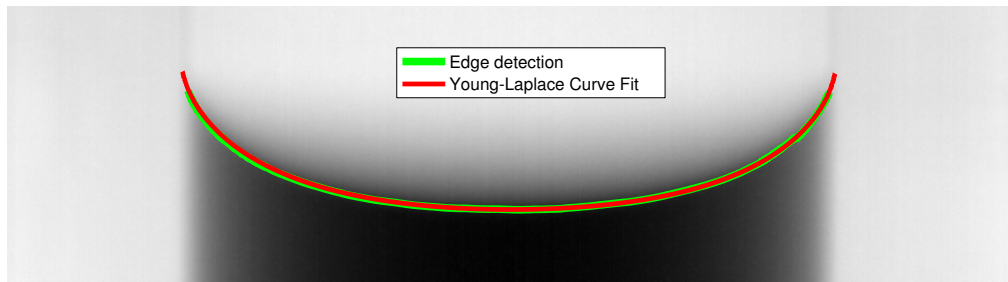


FIG. 7: Edge detected and Young–Laplace curves of liquid hydrogen in the 10 mm Al cell at 19.9 K

is the dimensionless height of the interface at a dimensionless distance r from the apex, λ is twice the curvature of the interface at the origin, Bo is the Bond number, θ is the contact angle, and $\psi = \tan^{-1}(df/dr)$. The equation is solved numerically using `ode113` (a variable order Adams–Bashforth–Moulton predictor–corrector solver in MATLAB). The equation is evaluated for a variable curvature at the origin and a least squares fit is performed. Once the appropriate Laplace curve is found for the interface, the contact angle is the value of the first derivative of f at $r = 1$. Figure 7 shows the edge detected curve in comparison with the fitted Young–Laplace curve. The analysis presented here suggests a contact angle of $0\text{--}4^\circ$ for hydrogen in contact with aluminum oxide. A description of the possible existence of a contact angle and the errors involved with measurement is discussed in Bellur et al. (2016a,b) and Konduru et al. (2016).

Within the limits of the imaging resolution, the curvature of the liquid vapor interface does not change during phase change. Hence the shape of the interface from the Laplace fit and the height of the meniscus apex from the inner bottom of the test cell are the only two parameters needed for accurate volume determination. All neutron images from a test run are processed through a $[5 \times 5]$ median filter and a $[5 \times 5]$ `sgolay` filter in MATLAB to remove stray neutron noise. Once a full meniscus is formed after condensation, the central scan described above is repeated on the entire image. The minimum of the quadratic fit provides the apex location needed for the volume determination. An axisymmetric 2D shape is constructed with the Laplace fit displaced by the apex height obtained for each image. The area and centroid of this 2D shape is determined using the trapezoidal rule and the volume is determined using Pappu’s second centroid theorem. The process is repeated for each image and the volume at every timestamp is logged.

4.2 Optical Density Method

The optical density method converts every pixel intensity (gray value) into a liquid thickness and thus relies on the intensity resolution. Every image with liquid is normalized with a dry image of the test cell (prior to condensation), the background image is removed and an attenuation coefficient for the liquid is measured. The coefficient is then used to transform the pixel intensities of the normalized image to a liquid transmission thickness using a modified Beer–Lambert equation. The liquid transmission thickness of the entire image is summed and multiplied with the pixel pitch to obtain the total volume.

In the images of the test cell just prior to condensation and just after evaporation, there is no visible liquid in the test cell but vapor at a set pressure is present. The attenuation from propellant vapor is not sufficient for visualization. These images are median combined to form a “reference”

image so that the only difference between the reference image and the test image is presence of the liquid propellant. Images with the neutron beam turned off were used to characterize the background radiation from the reactor. These images are median combined as well to form a “background” image.

As in the interface tracking method, further denoising routines are needed in addition to the deconvolution to remove the gamma noise. In this method, one must preserve most of the original pixel intensities and not intentionally blur the image with spatial filters to obtain a true volume from the original pixel intensities. Gamma noise or hot spots are randomly formed on every image and a temporal running median filter with a window of 3 images is used to remove them. Since the interface moves by less than 15 pixels in every test, a window of 3 images ensured that the temporal resolution is not severely affected. The filter is constructed such that the pixel intensities of a previous image, current image and next image is compared and a median value is chosen as the pixel intensity of the current image. This process is repeated for every pixel of every image of the test. The resulting images are mostly free of gamma noise and erratic jumps in intensity while preserving both spatial and temporal detail.

The processed neutron images from the phase change test (I_{TEST}) are converted into an optical density image (I_{OD}) by removing the background (I_B), normalizing resulting image with the reference image (I_{REF}). A logarithmic transform of the resulting normalization is the optical density image [Eq. (3)]. A sample optical density image of condensing hydrogen (temperature = 19 K, pressure = 120.6 kPa) in a 10 mm Al 6061 cell during the January 2015 tests is shown in Fig. 8:

$$I_{OD} = -\log\left(\frac{I_{TEST} - I_B}{I_{REF} - I_B}\right). \quad (3)$$

In order to account for the polychromatic neutron beam at the NIST BT-2 facility, a beam hardening correction must be applied to the exponential attenuation law to convert the optical density image into a liquid transmission thickness image

$$OD = \mu d + \beta d^2. \quad (4)$$

The coefficients to Eq. (4), μ and β are calculated from the sample optical density image by considering the horizontal line profile of optical density values along the condensed liquid (solid green line in Fig. 9). Assuming the test cell to be a perfect cylinder, the geometric thickness of the liquid (neutron transmission distance) can be calculated. The measured optical density is then fitted to the liquid thickness using the beam hardening model [Eq. (4)] to obtain the attenuation coefficient μ and beam hardening correction factor β for the particular test run. Figure 9 shows a line profile of optical densities along with the the geometric liquid thickness and the results of a beam hardening fit. Figure 10 shows the almost linear variation of optical density with liquid thickness with a slight second-order beam hardening correction. At low liquid thickness (<0.2 mm) the fit is bad due to the spatial resolution of neutron imaging combined with the quadratic nature of the film geometric film thickness. The quantities μ and β are weak functions of density and since pressure changes by less than 5 kPa during the course of an condensation/condensation test, the coefficients are assumed to remain constant and are only calculated once per test run. The attenuation coefficient calculated from optical density images for liquid hydrogen at 120 kPa is 1.431 which compares very well with the theoretically calculated coefficient of 1.437 (Table 1).

The calculated coefficients (μ and β) are then used to estimate a liquid transmission thickness value from every optical density pixel value using Eq. (4). The volume of liquid at each pixel is

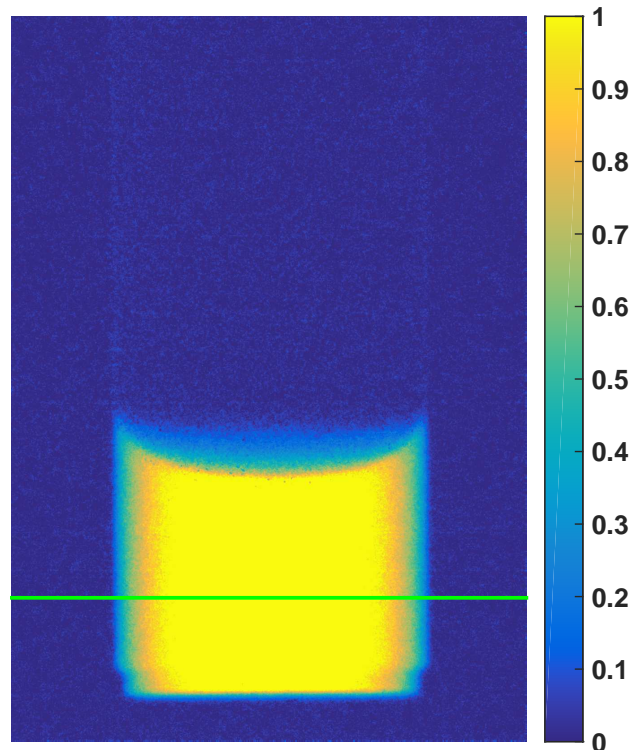


FIG. 8: Sample optical density image of condensed liquid hydrogen in the 10 mm Al 6061 cell from the January 2015 test

calculated based on each pixel's liquid transmission thickness and the pixel pitch. The volume of liquid in the entire image is summed based on the individual volumes represented by each pixel. Phase change rate can then be computed based on the liquid value from every image.

5. RESULTS AND DISCUSSION

Two different methods of measuring the volume of condensed liquid are discussed in the previous section. While the optical density method is robust to calculate volume from all images, the interface tracking method needs a fully formed meniscus for its use. Further, it was noticed in the September 2015 images with methane that condensation is seen on the top corner of the lid. The interface tracking method cannot compute the volume of this corner section and thus is only applicable when a single fully formed meniscus is seen. Condensation on the top corner was not captured in the January experiments due to the field of view of the imaging setup. The Young–Laplace fits in the interface tracking method suggests the possible existence of a finite contact angle. However, the optical density method shows that there exists a thin film of propellant on the walls of the test cell at all times. Figure 11(a) shows a sample image from the September 2015 test with condensed methane at 117.2 kPa and 110 K and Fig. 11(b) shows the line profile corresponding to the dashed red line. Condensation on the top corner is clearly observed and the line profile shows two clear peaks near the wall and an offset in optical density at the center of the cell. Both these features indicate a thin liquid film on the wall. The average thickness of the

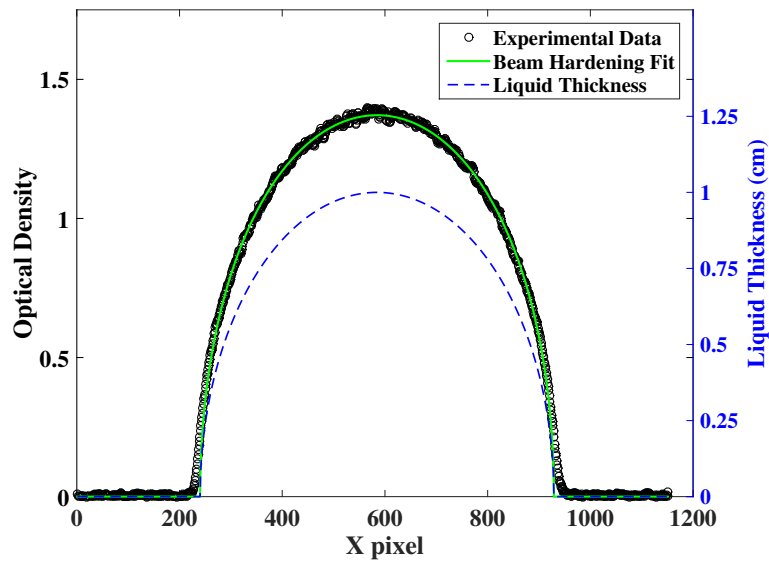


FIG. 9: Line profile of optical density along the liquid along with geometric liquid thickness (solid green line in Fig. 8)

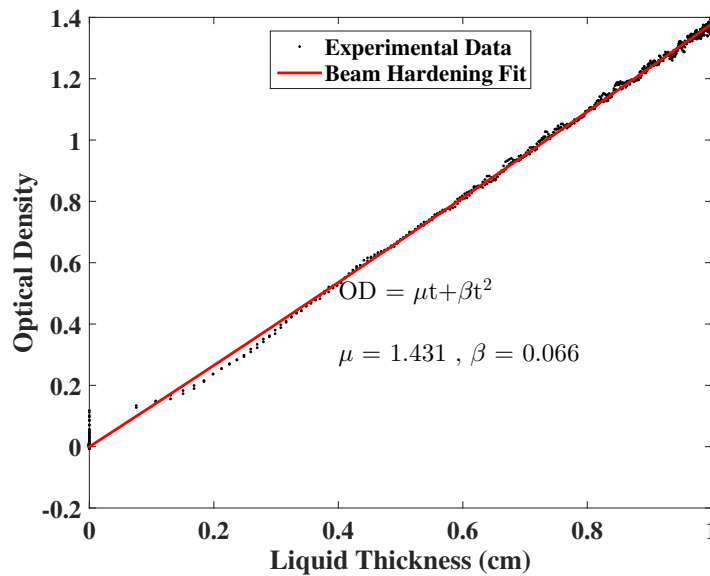


FIG. 10: Beam hardening fit to calculate attenuation coefficient

film in Fig. 11 is estimated to be 15 μm . It is the authors' hypothesis that the film thickness is a function of the condensation/evaporation rate and this will be explored in a future publication.

The temporal resolution of the measured volume is estimated to be $\pm 15.1 \text{ mm}^3$ due to the image exposure time of 10 s. This estimate is based on the maximum movement of the liquid meniscus (≈ 15 pixels) in consecutive images during the experiment. This temporal uncertainty applies to liquid volume determined by both methods described. Volume determination from

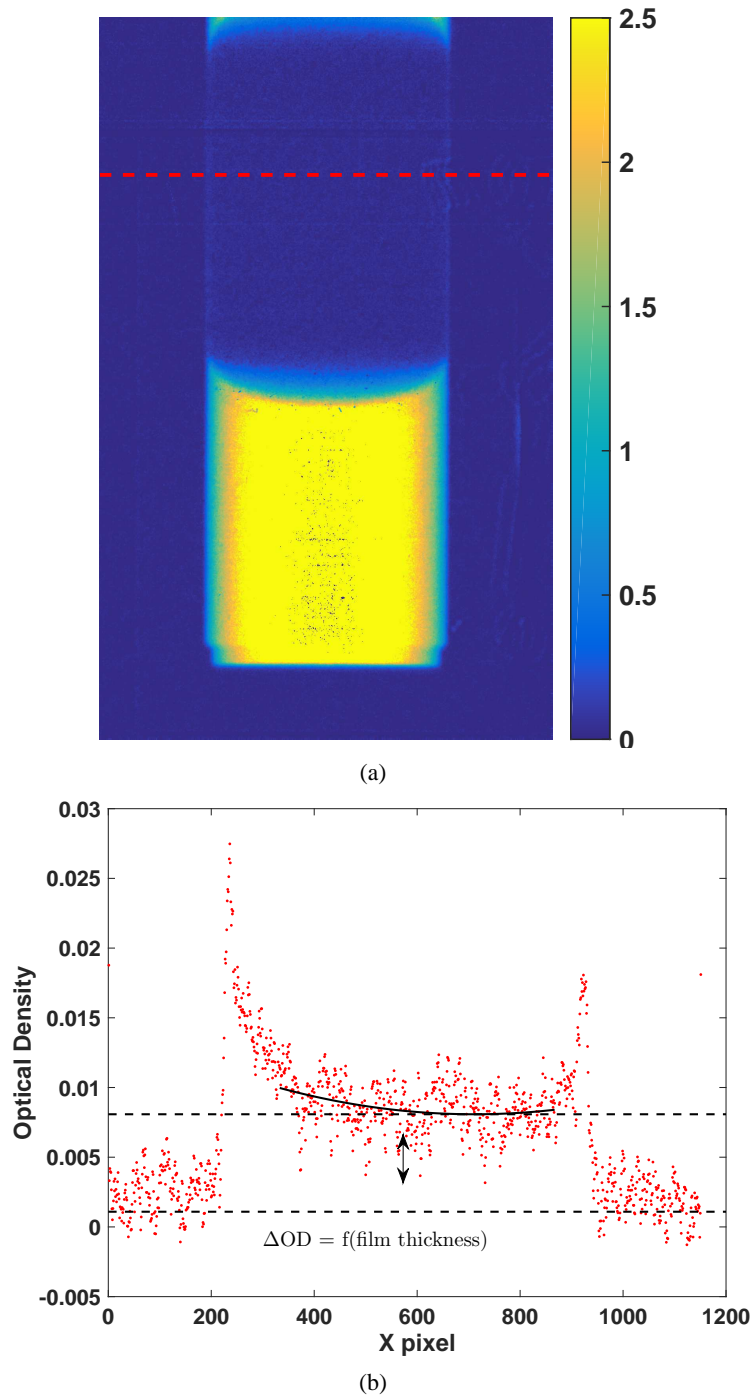


FIG. 11: Sample optical density image of condensed methane at 110 K and 117.2 kPa, from the September 2015 test (a) and the corresponding line profile scan along the dashed red line. (a) Sample optical density image, (b) line profile scan

the interface tracking method has additional uncertainty from edge detection, estimated to be a maximum of $\pm 5.7 \text{ mm}^3$ due to a ± 5 pixel error in interface detection. The errors add in quadrature and total uncertainty in the interface tracking volume measurement is $\pm 16.14 \text{ mm}^3$.

An additional uncertainty in the optical density method is based on neutron counting statistics in addition to the temporal uncertainty. Neutron transport to the imaging detector is a random process and the number of neutrons at a given time in a detector pixel is described by a Poisson distribution (Hussey et al., 2010). Ignoring the beam hardening correction and the uncertainty in the linear attenuation coefficient, the error in liquid volume from optical density can be estimated by the following equation:

$$\delta v = \frac{1}{\mu} \sqrt{\frac{2N}{I_o A T \eta}}, \quad (5)$$

where N is the number of pixels used to calculate the volume, $I_o = 5 \times 10^6 \text{ cm}^{-2} \text{ s}^{-1}$, the incident fluence rate, A is the area of each pixel, T is the exposure time, and η is the detection efficiency (0.8 for the GadOX screen used). The random error in the volume measurement with optical density method calculated from Eq. (5) is $\pm 0.56 \text{ mm}^3$ and the total uncertainty is $\pm 15.11 \text{ mm}^3$. Uncertainty in the volume measured from the edge detection method is about 6% greater than the volume uncertainty in the optical density method.

Figure 12 shows the results from one such test with hydrogen at saturated at 21 K in a 10 mm Al 6061 cell. The result corresponds to time lapse images in Fig. 3. Volume of liquid in the test cell based on neutron images is computed using both the interface tracking method and the optical density method and the agreement is very good.

6. SUMMARY

A new experimental technique to observe the liquid–vapor interface during phase change of cryogenic propellants is presented. Using the 70 mm orange cryostat and the BT-2 Neutron imaging facility at NIST, Gaithersburg, controlled phase change tests of liquid propellants were conducted and images of the liquid inside the opaque metallic containers were obtained through neutron transmission imaging. A new technique to accurately identify the liquid–wall interface has been determined using a simple exponential attenuation law. Two methods to determine condensed liquid volume are discussed and results are compared. The interface tracking method uses edge detection on a stacked image to compute the liquid vapor curvature and eventually measure the volume. The optical density method transforms every pixel gray value into liquid thickness and computes volume. Despite the fact that interface tracking method makes an assumption that the interface curvature is constant during a test, the measured volume agrees very well with the optical density measurement of volume. The volume measurement error with the interface tracking method is $\pm 16.14 \text{ mm}^3$ while the volume measurement with the optical density method is $\pm 15.11 \text{ mm}^3$, about 6% lower. The interface tracking method cannot be used unless a full meniscus is formed while the optical density method can work on any image. Further, the optical density technique can detect thin liquid films on the cell wall while the interface tracking method cannot. Hence, for an estimation of phase change rates from simple steady evaporation/condensation processes, an interface tracking method is shown to suffice but for high accuracy volume measurements and thin film analysis the optical density method should be preferred.

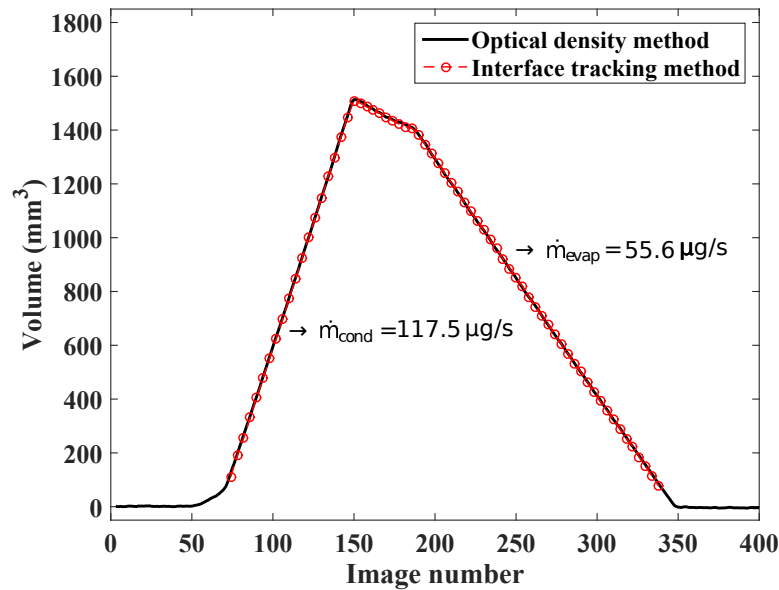


FIG. 12: Phase change rates for hydrogen in the 10 mm Al cell saturated at 21 K. Condensation test is conducted at 19 K and evaporation at 23 K

ACKNOWLEDGMENTS

This work was supported by an Early Stage Innovations Grant from NASA's Space Technology Research Grants Program (Grant # NNX14AB05G), the U.S. Department of Commerce, the NIST Radiation and Physics Division, the Director's office of NIST, and the NIST Center for Neutron Research. The authors wish to thank Eli Baltic, Juscelino B. Leão, Sergiy Gladchenko, Qiang (Alan) Ye, and Julia Scherschligt for their help in setting up the experiment and operating the cryogenic equipment. Certain trade names and company products are mentioned in the text or identified in an illustration in order to adequately specify the experimental procedure and equipment used. In no case does such identification imply recommendation or endorsement by the National Institute of Standards and Technology, nor does it imply that the products are necessarily the best available for the purpose.

REFERENCES

- Ajaev, V., *Interfacial Fluid Mechanics. A Mathematical Modeling Approach*, New York: Springer, 2012.
- Alberts, S.J., Srikanth, P., Collicott, S.H., and Heister, S.D., Experiment design for measuring accommodation coefficients for modeling of long-duration spaceflight cryogenic propellants, *13th Int. Energy Conversion Engineering Conf.*, Orlando, FL, p. 4246, July 23, 2015.
- Alberts, S.J., Srikanth, P., Collicott, S.H., and Heister, S.D., Numerical approach to measure accommodation coefficients for long-duration spaceflight cryogenic propellants, *52nd AIAA/SAE/ASEE Joint Propulsion Conf.*, Salt Lake City, UT, p. 4675, July 22, 2016.
- Barsi, S., Kassemi, M., Panzarella, C., and Alexander, J.I.D., A tank self-pressurization experiment using a model fluid in normal gravity, *43rd AIAA Aerospace Sciences Meeting and Exhibit*, Reno, NV, January 10, 2005.

- Bazylak, A., Liquid water visualization in PEM fuel cells: A review, *Int. J. Hydrogen Energy*, vol. **34**, no. 9, pp. 3845–3857, 2009.
- Bellur, K., Konduru, V., Kulshrestha, M., Tyrewala, D., Médiçi, E.F., Allen, J.S., Choi, C.K., Hussey, D.S., Jacobson, D.C., Leão, J.B., McQuillen, J., Hermanson, J., and Tamilarasan, A., Contact angle measurement of liquid hydrogen in stainless steel and aluminum cells, *J. Heat Transfer*, vol. **138**, no. 2, p. 020904, 2016a.
- Bellur, K., Médiçi, E.F., Kulshrestha, M., Konduru, V., Tyrewala, D., Tamilarasan, A., McQuillen, J., Leão, J.B., Hussey, D.S., Jacobson, D.L., Scherschligt, J., Hermanson, J., Choi, C., and Allen, J., A new experiment for investigating evaporation and condensation of cryogenic propellants, *Cryogenics*, vol. **74**, pp. 131–137, 2016b.
- Brenizer, J., A review of significant advances in neutron imaging from conception to the present, *Physics Procedia*, vol. **43**, pp. 10–20, 2013.
- Chadwick, M., Obložinský, P., Herman, M., Greene, N., McKnight, R., Smith, D., Young, P., MacFarlane, R., Hale, G., and Frankle, S., ENDF/B-VII.0: Next generation evaluated nuclear data library for nuclear science and technology, *Nuclear Data Sheets*, vol. **107**, no. 12, pp. 2931–3060, 2006.
- Cimbala, J.M., Brenizer, J.S., Chuang, A.P.Y., Hanna, S., Conroy, C.T., El-Ganayni, A., and Riley, D.R., Study of a loop heat pipe using neutron radiography, *Appl. Radiation Isotopes*, vol. **61**, no. 4, pp. 701–705, 2004.
- Concus, P., Static menisci in a vertical right circular cylinder, *J. Fluid Mech.*, vol. **34**, no. 03, pp. 481–495, 1968.
- Council, N.R., *NASA Space Technology Roadmaps and Priorities: Restoring NASAs Technological Edge and Paving the Way for a New Era in Space*, Washington, DC: The National Academies Press, 2012.
- Dewanckele, J., De Kock, T., Fronteau, G., Derluyn, H., Vontobel, P., Dierick, M., Van Hoorebeke, L., Jacobs, P., and Cnudde, V., Neutron radiography and X-Ray computed tomography for quantifying weathering and water uptake processes inside porous limestone used as building material, *Mater. Characteriz.*, vol. **88**, pp. 86–99, 2014.
- Fritz, D., Implementation of a phenomenological evaporation model into a porous network simulation for water management in low-temperature fuel cells, PhD thesis, Michigan Technological University, 2012.
- Hartmut, K. and Ernst, K., Photographic detection of slowly moving neutrons, US patent 2,186,757, filed March 24, 1938 and issued January 9, 1940.
- Hartwig, J. and McQuillen, J., Analysis of screen channel lad bubble point tests in liquid oxygen at elevated temperature, *42nd AIAA Thermophysics Conf.*, Honolulu, HI, June 27, 2011.
- Hartwig, J. and McQuillen, J., Analysis of screen channel lad bubble point tests in liquid methane at elevated temperature, *50th Aerospace Sciences Meeting*, Nashville, TN, January 9, 2012.
- Hartwig, J., McQuillen, J., and Chato, D., Performance gains of propellant management devices for liquid hydrogen depots, *51st Aerospace Sciences Meeting*, Grapevine, TX, January 7, 2013.
- Hussey, D., Jacobson, D., Arif, M., Huffman, P., Williams, R., and Cook, J., New neutron imaging facility at the NIST, *Nucl. Instr. Meth. Phys. Res. A*, vol. **542**, no. 1, pp. 9–15, 2005.
- Hussey, D., Jacobson, D., Arif, M., Coakley, K., and Vecchia, D., *In situ* fuel cell water metrology at the NIST neutron imaging facility, *J. Fuel Cell Sci. Technol.*, vol. **7**, no. 2, p. 021024, 2010.
- Kang, M., Bilheux, H.Z., Voisin, S., Cheng, C., Perfect, E., Horita, J., and Warren, J., Water calibration measurements for neutron radiography: Application to water content quantification in porous media, *Nucl. Instr. Meth. Phys. Res. A*, vol. **708**, pp. 24–31, 2013.
- Kihm, K., Kirchoff, E., Golden, M., Rosenfeld, J., Rawal, S., Pratt, D., Swanson, A., Bilheux, H., Walker, L., and Voisin, S., Neutron imaging of alkali metal heat pipes, *Physics Procedia*, vol. **43**, pp. 323–330, 2013.
- Konduru, V., Bellur, K., Médiçi, E.F., Allen, J.S., Choi, C.K., Hussey, D.S., Jacobson, D., Leão, J.B.,

- McQuillen, J., and Hermanson, J.C., Examining liquid hydrogen wettability using neutron imaging, *J. Heat Transfer*, vol. **138**, no. 8, p. 080901, 2016.
- Körner, S., Digital Image Processing in Neutron Radiography, PhD Thesis, Technische Univ. Wien, Vienna, 2000.
- Kramer, D., Zhang, J., Shimoi, R., Lehmann, E., Wokaun, A., Shinohara, K., and Scherer, G.G., *In situ* diagnostic of two-phase flow phenomena in polymer electrolyte fuel cells by neutron imaging: Part A. experimental, data treatment, and quantification, *Electrochimica Acta*, vol. **50**, no. 13, pp. 2603–2614, 2005.
- Panchamgam, S.S., Chatterjee, A., Plawsky, J.L., and Wayner, P., Comprehensive experimental and theoretical study of fluid flow and heat transfer in a microscopic evaporating meniscus in a miniature heat exchanger, *Int. J. Heat Mass Transfer*, vol. **51**, no. 21, pp. 5368–5379, 2008.
- Panzarella, C. and Kassemi, M., On the validity of purely thermodynamic descriptions of two-phase cryogenic fluid storage, *J. Fluid Mech.*, vol. **484**, pp. 41–68, 2003.
- Panzarella, C. and Kassemi, M., Self-pressurization of large spherical cryogenic tanks in space, *J. Spacecraft Rockets*, vol. **42**, no. 2, pp. 299–308, 2005.
- Panzarella, C. and Kassemi, M., One-dimensional model of evaporation and condensation in the presence of a noncondensable gas with applications to cryogenic fluid storage, *Int. J. Heat Mass Transfer*, vol. **52**, no. 15, pp. 3767–3777, 2009.
- Panzarella, C., Plachta, D., and Kassemi, M., Pressure control of large cryogenic tanks in microgravity, *Cryogenics*, vol. **44**, no. 6, pp. 475–483, 2004.
- Perfect, E., Cheng, C.L., Kang, M., Bilheux, H., Lamanna, J., Gragg, M., and Wright, D., Neutron imaging of hydrogen-rich fluids in geomaterials and engineered porous media: A review, *Earth-Sci. Rev.*, vol. **129**, pp. 120–135, 2014.
- Plawsky, J.L., Ojha, M., Chatterjee, A., and Wayner, P., Review of the effects of surface topography, surface chemistry, and fluid physics on evaporation at the contact line, *Chem. Eng. Commun.*, vol. **196**, no. 5, pp. 658–696, 2008.
- Preiss, G. and Wayner, P., Evaporation from a capillary tube, *J. Heat Transfer*, vol. **98**, no. 2, pp. 178–181, 1976.
- Satija, R., Jacobson, D.L., Arif, M., and Werner, S., *In situ* neutron imaging technique for evaluation of water management systems in operating PEM fuel cells, *J. Power Sources*, vol. **129**, no. 2, pp. 238–245, 2004.
- Von der Hardt, P. and Röttger, H., *Neutron Radiography Handbook: Nuclear Science and Technology*, Dordrecht, Holland: D. Reidel Publishing Company, 1981.
- Wayner, P., The effect of interfacial mass transport on flow in thin liquid films, *Colloids Surfaces*, vol. **52**, pp. 71–84, 1991.
- Wee, S.K., Kihm, K.D., Pratt, D.M., and Allen, J.S., Microscale heat and mass transport of evaporating thin film of binary mixture, *J. Thermophys. Heat Transfer*, vol. **20**, no. 2, pp. 320–326, 2006.
- Wilson, C., Borgmeyer, B., Winholtz, R., Ma, H., Jacobson, D., Hussey, D., and Arif, M., Visual observation of oscillating heat pipes using neutron radiography, *J. Thermophys. Heat Transfer*, vol. **22**, no. 3, pp. 366–372, 2008.